Scaling relations for granular flow in quasi-two-dimensional rotating cylinders

Ashish V. Orpe* and D. V. Khakhar†
Department of Chemical Engineering, Indian Institute of Technology–Bombay, Powai, Mumbai 400076, India
(Received 19 April 2001; published 27 August 2001)

An experimental study of the flow of different materials (steel balls, glass beads, and sand) in quasi-two-dimensional rotating cylinders is carried out using flow visualization. The flow in the rotating cylinder comprises of a thin-flowing surface layer with the remaining particles rotating as a fixed bed. Experimental results indicate that the scaled layer thickness increases with increasing Froude number ($\mathrm{Fr}=\omega^2 R/g$, where ω is the angular speed, R is the cylinder radius, and g the acceleration due to gravity) and with increase in size ratio ($s=d/R$, where d is the particle diameter). The free surface profile, is nearly flat at low Fr and becomes increasingly S shaped with increasing Fr. The layer thickness profiles, which are symmetric at low Fr become skewed at high values of Fr and small s. The dynamic angles of repose for all the materials studied show a near-linear increase with rotational speed (ω). Scaling analysis of the experimental data shows that the shape of the scaled surface profiles and the scaled layer thickness profiles are nearly identical when Froude number and size ratio are held constant, for each material. The surface profiles and layer thickness profiles are also found to be nearly independent of the material used. The dynamic angle of repose (β), however, does not scale with Fr and s and depends on the particle properties. The experimental results are compared to continuum models for flow in the layer. The models of Elperin and Vikhansky [Europhys. Lett. **42**, 619 (1998)] and Makse [Phys. Rev. Lett. **83**, 3186 (1999)] show good agreement at low Fr while that of Khakhar *et al.* [Phys. Fluids, **9**, 31 (1997)] gives good predictions over the entire range of parameters considered. An analysis of the data indicate that the velocity gradient ($\dot{\gamma}$) is nearly constant along the layer at low Fr, and the value calculated at the layer midpoint varies as $\dot{\gamma}_0 \propto [g \sin(\beta_0-\beta_s)/d \cos\beta_s]^{1/2}$ for all the experimental data, where β_s is the static angle of repose and β_0 is the interface angle at the layer midpoint. An extension of ''heap'' models (BCRE, BRdG) is used to predict the interface angle profiles, which are in reasonable agreement with experimental measurements.

DOI: 10.1103/PhysRevE.64.031302 PACS number(s): 45.70.Mg, 83.80.Fg

I. INTRODUCTION

Granular flows have been the subject of considerable research driven by both technological needs and the challenges of unresolved questions related to fundamental physics [1]. For example, flow equations for granular materials are not established and both discrete (particle dynamics, cellular automaton) and continuum (hydrodynamic equations) approaches have been developed for specific cases [2–5]. Industrial processes are thus based on designs, in many cases suboptimal, arrived at by experimentation and trial and error [6]. Fundamental studies using simple prototypical systems show promise for providing new insights that will contribute to the development of tools for rational design. An example of such a prototypical system is a rotating cylinder partially filled with granular material, which is the subject of the present paper. Rotating cylinders are also of considerable practical interest, since they are widely used in industry as drum mixers and rotary kilns [7,8].

The flow in the rotating cylinder can be divided into two regions: a flowing surface layer and a fixed bed rotating at the angular velocity of the cylinder. Henein *et al.* [9] identified several different flow regimes that occur with increasing angular speed of the cylinder: slipping, slumping or avalanching, rolling, cascading, cataracting, and centrifuging. Further, the transition between the avalanching and rolling regimes was found to be dependent on the Froude number ($\mathrm{Fr}=\omega^2 R/g$, where ω is the angular speed, R is the cylinder radius, and g the acceleration due to gravity) and the size ratio ($s=d/R$, where d is the particle diameter). Several experimental studies have considered different aspects of the rotating cylinder flow and we review these below.

Rajchenbach [10] in an early work, showed the dynamic angle of repose (the angle of the free surface, β, see Fig. 1) to vary with rotational speed (ω) as $(\beta-\beta_s)\propto\omega^2$ for small $(\beta-\beta_s)$, where β_s is the static angle of repose. Dury *et al.* [11] investigated the effects of the end walls on the dynamic angle of repose by means of computations, magnetic resonance imaging (MRI), and flow visualization. They found the angle at the end walls to be higher by 4°–5° than at the center. A characteristic length for decay of the angle was determined, which scaled with cylinder radius, but was independent of the particles and gravitational constant. The angle β away from the ends was found to vary linearly with the rotational speed. A similar variation of β with rotational speed was reported by Yamane *et al.* [12] using MRI. More recently, Khosropour *et al.* [13], considering a wider range of rotational speeds, obtained a slower than linear increase in β with rotational speed. At the higher rotational speeds, the surface becomes S-shaped, hence, the dynamic angle of repose is not well defined. In the studies discussed above, β is

*Email address: avorpe@che.iitb.ac.in
†Author to whom all correspondence may be addressed. Email address: khakhar@che.iitb.ac.in

 ©2001 The American Physical Society

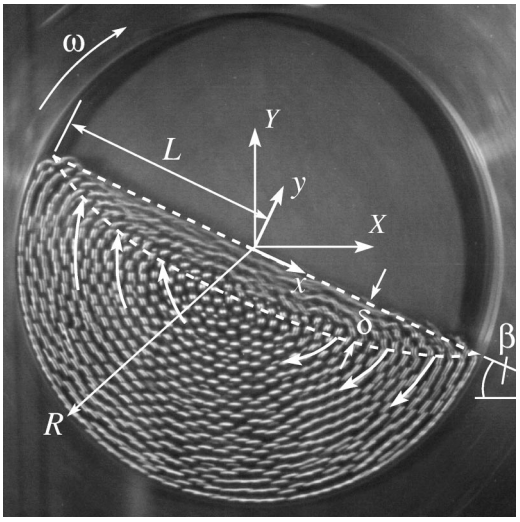

FIG. 1. Typical streakline photograph for 4 mm steel balls rotated in a cylinder of radius 8 cm for $\mathrm{Fr}=2\times10^{-3}$. Dashed lines show the free surface and the bed-layer interface. The coordinate system used in the model is also shown.

generally taken to be the angle near the midpoint of the layer.

A detailed study of the flow was carried out by Nakagawa *et al.* [14] using MRI. They obtained a near linear velocity profile in the flowing layer [see Eq. (1) below]. A similar variation of the velocity was obtained by Rajchenbach *et al.* [15] in a two-dimensional (2D) rotating cylinder using image analysis. Further, they showed that the scaled velocity and density profiles, for different rotational speeds were identical. Khakhar *et al.* [16] studied the flow behavior in quasi-2D cylinder and obtained layer thickness profiles using flow visualization. Boateng and Barr [17] used optical probes to obtain velocity, density, and temperature profiles in 3D cylinders. In all cases, with the exception of Boateng and Barr [17], experimental systems are small. Further, system sizes have not been varied, and it is not clear how results are affected with change in the system size. The effect of different material types on the flow also does not appear to be known.

Several models have been proposed to describe the flow in the cylinder [10,16,18–21]. All models are based on depth averaged hydrodynamic equations, but differ primarily in choice of the constitutive equation for the stress. We review recent models in the following section. A detailed comparison of model predictions to experiments has not been previously made.

We report here on an experimental study of flow in quasi-2D rotating cylinders using flow visualization. Particle size, particle material, cylinder size, and cylinder rotational speed are varied. The primary objective of the paper is to obtain scaling relations for the systems studied, in terms of the system parameters. The experimental results obtained are also compared to recent continuum models described in the next section. Experimental details are given in Sec. III, and the results are presented in Sec. IV. The conclusions of the paper are summarized in the final section.

II. CONTINUUM MODELS

Several models have been proposed to describe the flow in the layer, schematically shown in Fig. 1. Rajchenbach [10] calculated the dynamic angle of repose near the layer midpoint ($x=0$) considering the stress to be a linear sum of collisional and frictional stresses, and the layer thickness at $x=0$ to be nearly independent of the rotational speed. Rao *et al.* [18] developed a model for the complete flow but considered only frictional stresses. Zik *et al.* [19] assumed a constant layer thickness to compute the shape of the free surface. Khakhar *et al.* [16], Elperin and Vikhansky [20] and Makse [21] developed models for the complete flow and we review these below.

Khakhar *et al.* [16] obtained depth averaged steady-state mass and momentum balance equations. In the development, the flow is assumed to be in the rolling regime and the shape of the free surface is considered to be nearly flat. The shear stress is taken to be a sum of the frictional and the collisional stresses, with the frictional forces assumed to be of the Coulombic form, and Bagnold's [22] result is used to model the collisional stresses. The particle pressure along the flow direction is considered to be constant and the velocity is assumed to vary linearly with the distance across the layer, as

$$v_x = 2u\left(1+\frac{y}{\delta}\right), \tag{1}$$

where $u=(1/\delta)\int_{-\delta}^{0} v_x\,dy$ is the average velocity in the layer. Further, the density in the layer is assumed to be constant and nearly equal to the bed density.

The governing equations for the flow are the dimensionless momentum balance equation, after simplification given by

$$\frac{1}{2}\frac{d(\overline{u^2})}{d\xi} = \left[\frac{3}{4}\left(\frac{A\overline{R}}{\mathrm{Fr}}-\frac{A_1\overline{R}}{\mathrm{Fr}}\frac{\xi}{\overline{u}}\right)+\xi\frac{\overline{u^2}}{\overline{Q}}-3\alpha_S\frac{\overline{u^4}}{\overline{Q^2}}\right] \times\left[1+\frac{3A_1}{4\mathrm{Fr}}\frac{\overline{RQ}}{\overline{u^3}}\right]^{-1}, \tag{2}$$

and the dimensionless mass balance that yields the dimensionless flow rate,

$$\overline{Q}=\overline{u}\,\overline{\delta}=\frac{1}{2}[1-\xi^2]. \tag{3}$$

In the above equations, $\overline{u}=u/\omega L$ is the dimensionless mean velocity along the layer, $\overline{\delta}=\delta/L$ is the dimensionless layer thickness, $\xi=x/L$ is the dimensionless distance along the flow direction, and $\overline{R}=R/L$ is the dimensionless radius of the cylinder. The scaled net body force (i.e., gravitational force less frictional resistance) per unit weight acting on the layer is determined by the parameter $A=(\tan\beta-\tan\beta_s)\cos\beta$. The effective coefficient of dynamic friction is assumed to be $\tan\beta_s$, where β_s is the static angle of repose. The parameter $A_1=\sin\beta\tan\beta_s$ is a correction term to account for the variation in layer thickness and is $O(\delta')$.

It has only a small effect on the flow profile [16]. Both parameters depend on β and β_s and thus on the rotational speed of the cylinder. The dimensionless rotational speed is defined in terms of Froude number ($\mathrm{Fr}=\omega^2 R/g$). The flow in the layer is damped by the collisional stresses, the magnitude of which is determined by the dimensionless parameter, α_S. Here we take α_S to be a fitting parameter of the model. Both angles β and β_s are measured, as detailed below. Equations (2) and (3) are solved to determine the variation of average velocity ($\overline{u}$) and layer thickness ($\overline{\delta}$) along the flow direction (ξ).

Elperin and Vikhansky [20] developed a similar model for flow in the layer; two primary differences are (i) the stress in the flowing layer is assumed to be purely collisional (no friction) and (ii) the Mohr-Coulomb failure criterion is applied at the interface. The latter yields $\delta^3 \propto u^2$, and an analytical expression for the layer thickness profile is obtained as

$$\overline{\delta}=\left(\frac{\Omega}{2}\right)^{2/5}(1-\xi^2)^{2/5}, \tag{4}$$

where Ω is the dimensionless angular velocity, treated as a fitting parameter.

Makse [21] also proposed a model for the flow in the layer. Only the mass balance (Eq. 3) is used together with the assumption of a constant shear rate ($\dot{\gamma}$), which implies a linear variation of mean velocity with layer thickness ($u \propto \delta$). The layer thickness profile in this case is

$$\overline{\delta}=\left(\frac{\omega}{\dot{\gamma}}\right)^{1/2}(1-\xi^2)^{1/2}, \tag{5}$$

where the shear rate is a fitting parameter. This result is shown to be in agreement with the experimental data of Nakagawa *et al.* [14] and Khakhar *et al.* [16].

Zik *et al.* [19] and Elperin and Vikhansky [20] proposed models for calculating the free surface shape using a Mohr-Coulomb failure criterion at the interface. Phenomenological heap models [23,24] suggest that the local angle is determined by the local interchange rate between the flowing layer and the fixed bed. Thus, for ''thick'' layers, the surface angle can be written as [24]

$$\beta=\beta_m-\frac{\Gamma}{V}, \tag{6}$$

where Γ is the interchange rate between the layer and the fixed bed, V is a characteristic velocity, and β_m is the angle of the interface at which there is no interchange ($\Gamma=0$). Continuum models, similar to the model of Khakhar *et al.* [16] described above, together with a Mohr-Coulomb type failure criterion at the interface, yield an identical result for the surface angle with $V=g/\dot{\gamma}\cos\beta_m$ [25,26]. In addition, β_m is shown to be the effective angle of static friction [25,26]. Following Rajchenbach [27], Douady *et al.* [25] proposed that the shear rate should be constant and given by

$$\dot{\gamma}=(g\sin\beta/d)^{1/2}. \tag{7}$$

Recent experimental results [26] support the above model, but indicate that β_m depends on the local flow rate. Further, a different expression for $\dot{\gamma}$ is obtained [26]

$$\dot{\gamma}=\left[\frac{g\cos\beta\sin(\beta_m-\beta_s)}{\alpha_S R\cos\beta_m\cos\beta_s}\right]^{1/2}. \tag{8}$$

We apply Eq. (6) to the case, of a rotating cylinder. In this case the interchange rate is $\Gamma=\omega x$. Using Eq. (3), the scaled shear rate for a linear velocity profile [Eq. (1)] is given by

$$\dot{\gamma}/\omega=2\overline{u}/\overline{\delta}=(1-\xi^2)/\overline{\delta}^2. \tag{9}$$

Substituting this result in Eq. (6), together with the expression for V, we get

$$\beta_x=\beta_m-\xi(1-\xi^2)\left(\frac{\mathrm{Fr}\cos\beta_m}{R\overline{\delta}^2}\right), \tag{10}$$

where β_x is the angle of the *interface* at positions along the flowing layer.

III. EXPERIMENTAL DETAILS

Quasi-2D acrylic cylinders (length 1 or 2 cm) with three different radii ($R=4$, 8, and 16 cm) and transparent acrylic end walls are used. A computer controlled stepper motor with a sufficiently small step is used to rotate the cylinder. Steel balls of three sizes, 1, 2, and 4 mm, glass beads of four different sizes, 0.8, 1, 2, and 4 mm, and sand particles of two sizes, 0.4 and 0.8 mm, are used in the experiments. The steel balls are highly spherical, the glass beads are nearly spherical, and the sand particles are of irregular shape. Narrow cuts of all the particles are obtained by sieving. Specially fabricated perforated plate sieves were used for the 1, 2, and 4 mm particles, and for a cut of size d a pair of sieves with circular holes of diameter $(d-0.2)$ mm and $(d+0.2)$ mm were used. Standard sieves were used for the 0.4 mm (Tyler Nos. 20 and 24) and 0.8 mm (Tyler Nos. 35 and 42) particles.

The flow is intermittent for 4 mm particles in the cylinder of length 1 cm. This is because the flowing layer width is only 2–3 particle diameters and the wall effects become significant. When a 2 cm long cylinder is used for the 4 mm particles (flowing layer width is five particle diameters), this problem is eliminated and a smooth and steady flow is obtained. As shown below, further increase in the cylinder length does not modify the flow. Thus, cylinders of length 2 cm were used for 4 mm particles and of length 1 cm for the other particles. Static charge, which is significant for small particles, was eliminated using an antistatic solution (Filtec, India). The fill fraction used in all the experiments is 50%.

Time-exposed photographs of the rotating cylinder (Fig. 1), are taken at sufficiently low shutter speeds (1/4 to 1/30 s) so as to obtain particle streaklines. The corners of the streaklines in the image, which represent the transition between the fixed bed and the cascading layer flow, are joined to obtain the lower boundary of the layer. Similarly, a line is drawn

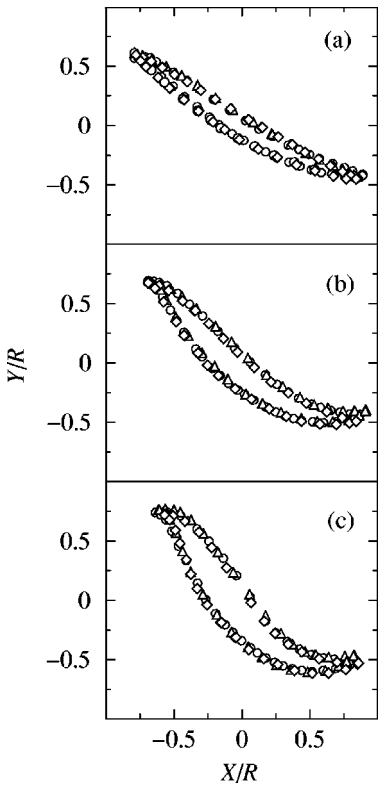

FIG. 2. Effect of end walls on the surface profiles. Symbols denote experimental data for 2 mm steel balls in a cylinder of radius $R=8$ cm for different cylinder lengths and end walls: ○, 1 cm thick cylinder with acrylic end walls; △, 1 cm-thick cylinder with back wall of aluminum; ◇, 2 cm thick cylinder with acrylic end walls. Data are shown for three different Froude numbers (Fr). (a) Fr $=2\times10^{-3}$, (b) Fr$=22\times10^{-3}$, and (c) Fr$=64\times10^{-3}$.

along the free surface (Fig. 1). A polynomial of degree 10 is fitted to each of these curves, scaling distances with respect to R, and with the origin of the coordinate system at the axis of the cylinder. The scaled layer thickness profile, $\delta(x/L)/R$, defined as the perpendicular distance from the free surface to the bed-layer interface, is obtained computationally from the polynomials. Here, x is the distance along the free surface and $2L$ is the length of the free surface. Each layer thickness profile is averaged over six images. The dynamic angle of repose (β) is taken to be the slope of the free surface curve at the point where the layer thickness is maximum. Experiments are carried out at several different Froude numbers (Fr) for each cylinder. For all the Froude numbers studied, the flow is in the rolling regime or the cascading regime [9]. The static angle of repose (β_s) is taken to be the angle of the stationary free surface that results when the rotation of the cylinder, operating under steady flow conditions, is stopped.

To estimate the magnitude of wall effects, we carried out experiments with 2 mm steel balls in cylinders of radius 8 cm and lengths 1 and 2 cm (5 and 10 particle diameters) with acrylic end walls, and using a 1 cm long cylinder with one end wall of aluminum and one of acrylic. The flowing layer profiles in these three cases are the same within experimental error as shown in Fig. 2 for different Froude numbers. The

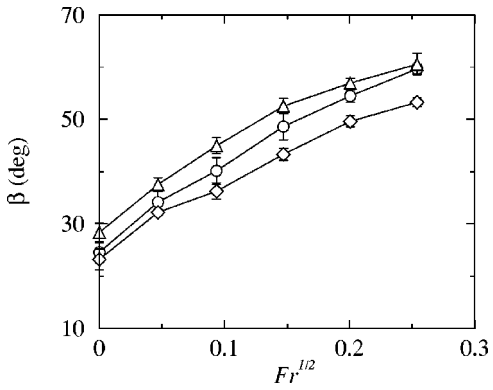

FIG. 3. Variation of the dynamic angles of repose (β) with dimensionless rotational speed ($\mathrm{Fr}^{1/2}$) to show the effect of the end walls. Symbols denote experimental values for 2 mm steel balls as defined in Fig. 2.

traced interface and free surface profiles are superimposed in Fig. 2, after rotating by the difference in the dynamic angles of repose, which vary as shown in Fig. 3. Thus, measurements of the layer thickness profiles are not significantly affected by the end walls. The angle of repose for the case with a back plate of aluminum is the highest, while that for the 2 cm long cylinder is the lowest, for a fixed Froude number (Fig. 2). Although the orientation of the surface profiles is slightly different in each case, this does not affect the flow.

The above results may seem surprising, since from a microscopic viewpoint (particle length scale), the density distribution and other dynamic variables are quite different near the wall as compared to the bulk. At the macroscopic scale (layer length scale), however, the primary effect of the end walls is to impose a tangential friction force. For high-bulk density flows, as considered in this paper, this wall friction is small (end walls are smooth) relative to the interparticle friction and collisional forces, which dominate the flow. Consequently, velocity gradients normal to the end walls are negligibly small. The tangential friction force changes the dynamic angle of repose by a small amount ($4°-5°$) which alters the magnitude of the gravitational driving force only slightly. Model computations show that change in the dynamic angle of repose by 5° alters the layer thickness profile very slightly. Thus, the flow in the layer is unaffected by the walls on a macroscopic scale, and the thickness profiles at the walls should be the same as those in the interior.

IV. RESULTS AND DISCUSSION

We first present experimental results to illustrate the effect of particle size, cylinder size, and rotational speed on the flow for a given material. This is followed by results showing the effect of the material properties on the experimental measurements. Scaling relations are discussed in each case. Comparisons of the experimental data with predictions of the models is shown next.

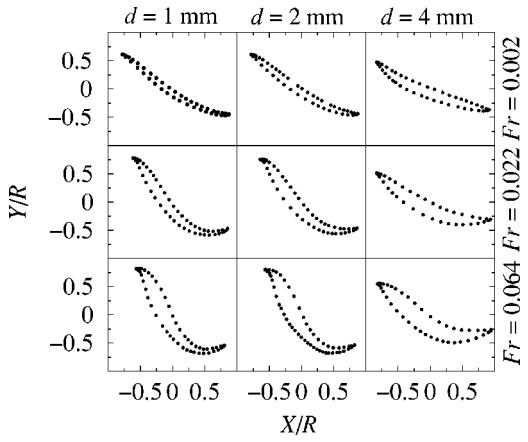

FIG. 4. Scaled layer shape profiles for three different sized steel balls rotated in a cylinder of radius 16 cm for three different Froude numbers as indicated.

A. Effect of rotational speed, particle size, and cylinder size

The experimentally obtained free surface and bed-layer interface profiles, demarcating the surface flowing layer, are shown in Fig. 4 for steel balls of different sizes in a cylinder of radius 16 cm, and in Fig. 5 for 2 mm steel balls in cylinders of different sizes. In each case, profiles are shown for three different Froude numbers spanning the range of rotational speeds studied. The results show that the maximum layer thickness increases and the free surface becomes more *S* shaped with increasing rotational speed. Further, with decreasing size ratios ($s=d/R$) the scaled maximum layer thickness decreases and the surface becomes more *S* shaped. The occurrence of an *S*-shaped profile at higher rotational speeds is usually attributed to inertial forces. However, in the cases studied here, *S*-shaped profiles are obtained even at the lowest rotational speeds for the largest cylinders. At these rotational speeds, inertial forces are negligible relative to gravitational forces, with Froude numbers $O(10^{-3})$. The *S*-shaped profiles result from a varying interchange rate between the bed and the layer (Γ) and a varying angle of friction along the bed-layer interface (β_m), and we discuss this in more detail below.

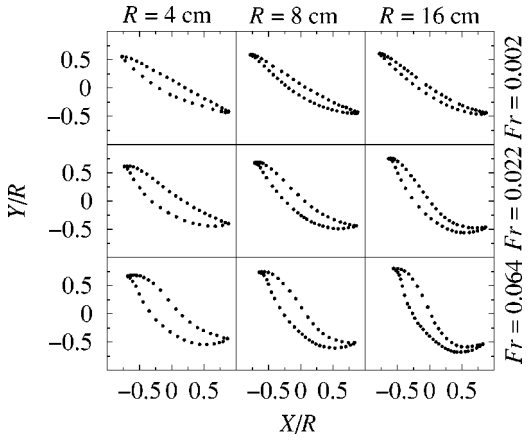

FIG. 5. Scaled layer shape profiles for 2 mm steel balls rotated in three different sized cylinders for three different Froude numbers as indicated.

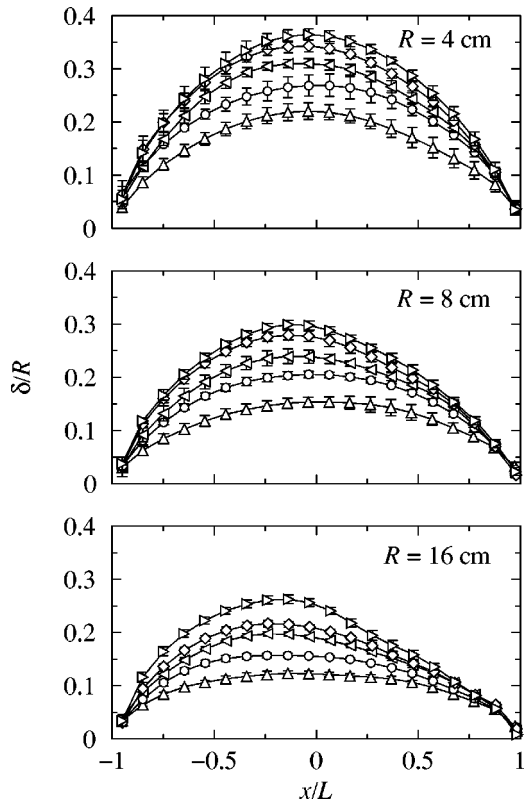

FIG. 6. Scaled layer thickness profiles for 2 mm steel balls in cylinders of different radii (R). Symbols denote experimental data for different Froude numbers (Fr): △, Fr$=2\times10^{-3}$; ○, Fr $=9\times10^{-3}$; ◁, Fr$=22\times10^{-3}$; ◇, Fr$=40\times10^{-3}$; and ▷, Fr $=64\times10^{-3}$.

The layer thickness profiles extracted from the outlines give a more detailed view of the flow. Figure 6 shows the variation of the scaled layer thickness with distance along the free surface for 2 mm steel balls in cylinders of different radii. Data is shown for five different Froude numbers in each case. The error bars show the standard deviation over six measurements, which is small in all cases. The results indicate that the maximum layer thickness increases with Froude number for a fixed cylinder size. The profiles are symmetric about the midpoint ($x=0$) at low Froude numbers, and become increasingly skewed at higher Froude numbers, with the maximum shifting to the upper part of the flowing layer. The maximum layer thickness increases significantly with cylinder size for a fixed Froude number, but when scaled with the cylinder radius, it decreases slightly with increasing cylinder size (Fig. 6). At the higher Froude numbers, the skewness of the profiles increases with the cylinder size. Qualitatively similar results are obtained for all the other materials studied. In all the cases, the length of the free surface ($2L$) increases with Fr due to curvature of the surface. For the range of Froude numbers studied, L/R varies from 1.0 to 1.15.

The variation of the dynamic angle of repose (β, the surface angle at the point where the layer thickness is maximum) with dimensionless rotational speed ($\mathrm{Fr}^{1/2}$) is shown in Fig. 7 corresponding to the data shown in Fig. 6. The points at Fr$=0$ correspond to the static angles of repose

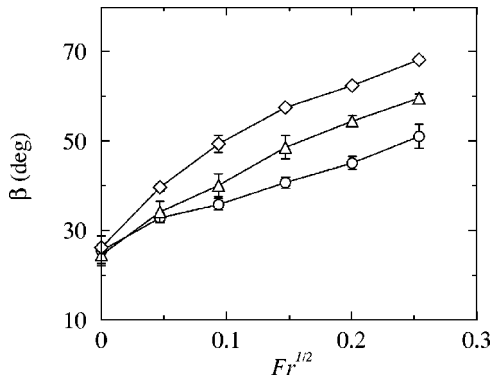

FIG. 7. Variation of the dynamic angle of repose (β) with dimensionless rotational speed ($Fr^{1/2}$). Symbols denote experimental data for 2 mm steel balls rotated in cylinders of three different radii: ○, R=4 cm; △, R=8 cm; and ◇, R=16 cm.

(β_s). There is a near-linear increase of the dynamic angle of repose with rotational speed. At a fixed Froude number, the dynamic angle of repose increases with cylinder size (Fig. 7). Experimental results for other systems indicate that smaller particles generally have larger dynamic angles of repose for fixed Fr and cylinder size. The dynamic angle of repose is larger for sand as compared to steel balls and glass beads, which have comparable dynamic angles of repose.

The results presented above clearly indicate that the flow in the layer does not scale with the Froude number alone. However, as we show below, if both Froude number and size ratio are kept constant, very good scaling is obtained. For example, Fig. 8 shows the scaled surface and interface profiles for cylinders of two different sizes and steel balls of two sizes, such that the size ratio is $s=1/80$. The layer shape profiles for the two cases, rotated by the difference in the dynamic angles of repose, are nearly identical. The scaling holds for all the Froude numbers studied and the complex shapes obtained are well reproduced. Figure 9 shows the scaled layer thickness profiles for three size ratios and three Froude numbers for the steel balls. The scaled profiles are the same, within the experimental error, for the different systems studied when the Froude number and size ratio are the same. The dynamic angle of repose, however, does not scale with these two parameters as shown in Fig. 10.

Qualitatively similar results are obtained for glass beads. Sand, in spite of its nonuniform shape, also shows a similar scaling and typical results are shown in Figs. 11 and 12, for the layer outlines and the layer thickness profiles, respectively. The dynamic angle of repose does not scale with Fr and s in this case either (Fig. 13).

A quantitative estimate of the validity of the scaling was obtained by calculating the average standard deviation of layer thickness profiles, for a fixed Fr, s and a given material, from the average profile for that case. The average standard deviation normalized by the particle diameter is given in Table I for all the cases studied. In all cases (except for the two cases involving sand) the standard deviation is less than one particle diameter.

The results presented indicate that the flow in the layer is essentially determined by the Froude number and size ratio.

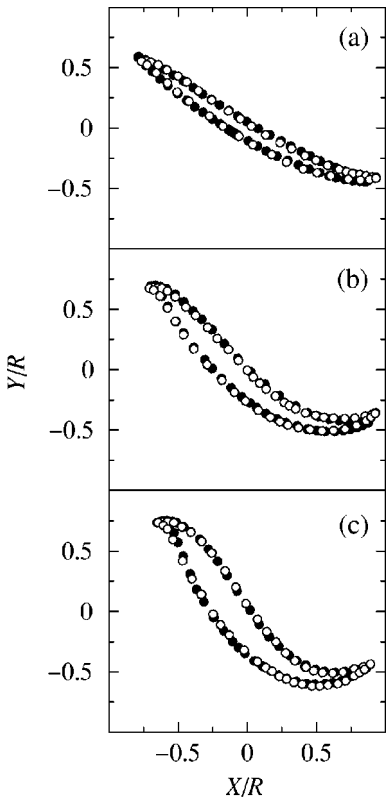

FIG. 8. Scaled layer shape profiles of steel balls for a size ratio $s=1/80$ for three different Froude numbers. (a) $Fr=2\times10^{-3}$, (b) $Fr=22\times10^{-3}$, and (c) $Fr=64\times10^{-3}$. Open symbols, $R=8$ cm, $d=1$ mm; filled symbols, $R=16$ cm, $d=2$ mm.

When these parameters are kept constant, not only the layer thickness profiles but also the details of the complex shapes of the free surface and interface are well reproduced in systems of different sizes. Such results have not been previously reported. The dynamic angle of repose, however, appears to be dependent on the particle surface properties and hence does not scale.

B. Effect of material type

We compare next the flow in the cylinder for the different materials studied. Figure 14 shows the outlines of the flowing layers for 2 mm glass beads and 2 mm steel balls in a cylinder of radius 16 cm superimposed on each other. As before, one of the profiles is rotated by the difference in the dynamic angle of repose. The profiles are remarkably similar. Figure 15 shows a comparison of the layer thickness profiles for three different size ratios and Froude numbers. The agreement is reasonably good in all cases, but is better for the higher Froude numbers studied.

Comparisons between profiles for sand and glass beads of the same size (0.8 mm) are shown in Figs. 16 and 17. The outlines in the two cases are very similar. The layer thickness profiles show some differences at lower Froude numbers and beyond the layer midpoint ($x>0$). The differences, however, are not too large.

The results presented here indicate that to reasonable approximation, the flow in the layer is independent of the ma-

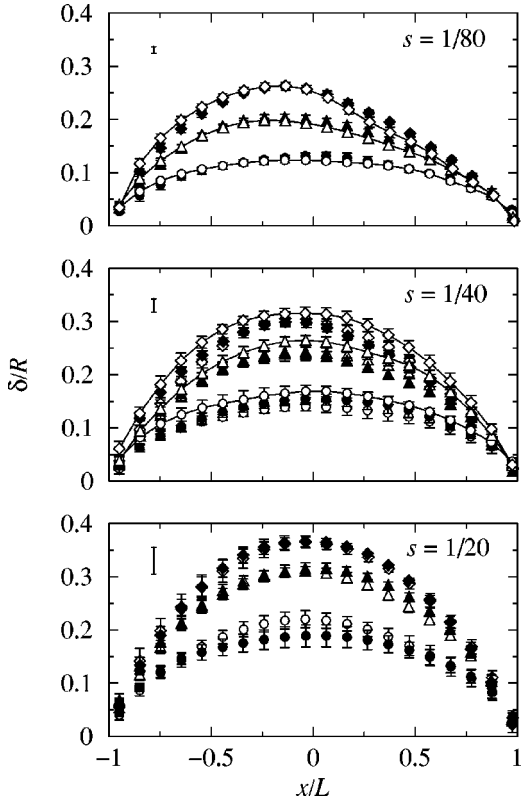

FIG. 9. Scaled layer thickness profiles for steel balls. Symbols denote experimental data for different Froude numbers (Fr) and size ratios (s): ○, Fr$=2\times10^{-3}$; and △, Fr$=22\times10^{-3}$; ◇, Fr $=64\times10^{-3}$. Open symbols, $R=4$ cm; filled symbols, $R=8$ cm; open symbols with solid line, $R=16$ cm. The bar indicates the size of a particle.

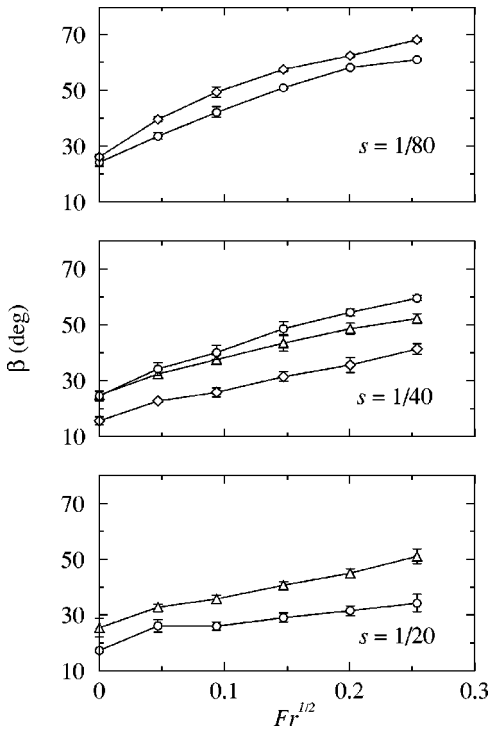

FIG. 10. Variation of the dynamic angle of repose (β) with dimensionless rotational speed ($\mathrm{Fr}^{1/2}$) for different size ratios (s). Symbols denote experimental data for steel balls rotated in cylinders of three different radii: △, $R=4$ cm; ○, $R=8$ cm; and ◇, $R=16$ cm.

terial type and depends only on the Froude number and particle size. Parameters such as coefficients of restitution and particle roughness appear to have only a minor effect on the flow. Steel balls, glass beads, and sand all have different shapes, however, within this range of variation (all are rounded), shape also has little effect on the flow. The primary effect of these parameters is on the dynamic angle of repose which is different for the different materials.

C. Comparison to theory

We compare the prediction of different theories to experimental results for the layer thickness profiles and interface shapes in this section. The theories by Elperin and Vikhansky [20] and Makse [21] both predict symmetric profiles. A comparison of the theoretical predictions with the data at the lowest Froude number studied is shown in Figs. 18 and 19 (dashed and dotted lines) for steel balls and sand, respectively. The predictions of the two models are nearly indistinguishable, and match well with the experimental data (the deviation is less than one particle diameter). However, the models cannot describe the skewed profiles obtained at the higher Froude numbers. In both models, the fitting parameters $(\Omega, \dot{\gamma})$ are obtained from the value of the layer thickness at the midpoint $[\overline{\delta}(0)]$.

Figures 18 and 19 also show the predictions of the model of Khakhar *et al.* [16] (solid lines). The fitting parameter (α_S) was adjusted to obtain the best fit for each data set studied. The fitted values of α_S for all Fr, s, and materials used were found to vary linearly with size ratio ($\alpha_S = Ms$). A least squares fit using all 90 experimental data sets (each set an average of 6 measurements) gave $M=1.53\pm0.12$, and the reported calculations are based on this correlation. The data in the figures span Froude numbers from 2×10^{-3} to 64×10^{-3}, size ratios from 0.05 to 0.005 and two particle shapes: perfectly spherical (steel balls) and irregular (sand). The agreement is good in all cases and deviations are less than one particle diameter in most cases. The deviations are highest at the highest Froude numbers and these could be due to curvature effects and dilation of the layer with flow, both of which are neglected in the model. The skewness of the computed profiles is also slightly larger than the experimental profiles for the steel balls. The agreement is expectedly better when the model is fitted to each profile instead of using the correlation. At low Froude numbers the profiles from the model of Khakhar *et al.* [16] are nearly identical to those of Elperin and Vikhansky [20] and Makse [21].

In Khakhar *et al.* [16], it was shown that the continuum model describes experimental data for layer thickness profiles well, however, the experimental system used was small ($R=7$ cm) and the effect of particle size was not systematically investigated. The experimental results presented here extend the conclusions of the previous work over a much wider range of conditions. Further, the fitted correlation for

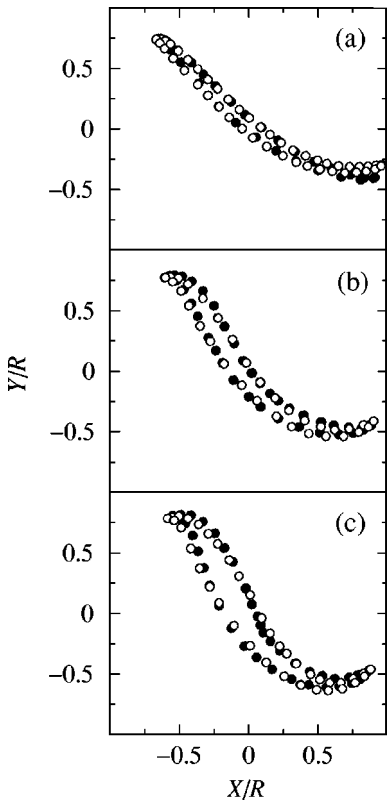

FIG. 11. Scaled layer shape profiles of sand particles for a size ratio $s=0.4/80$ for three different Froude numbers: (a) Fr $=2\times10^{-3}$, (b) Fr$=22\times10^{-3}$, and (c) Fr$=64\times10^{-3}$. Filled symbols, $R=8$ cm, $d=0.4$ mm; open symbols, $R=16$ cm, $d=0.8$ mm.

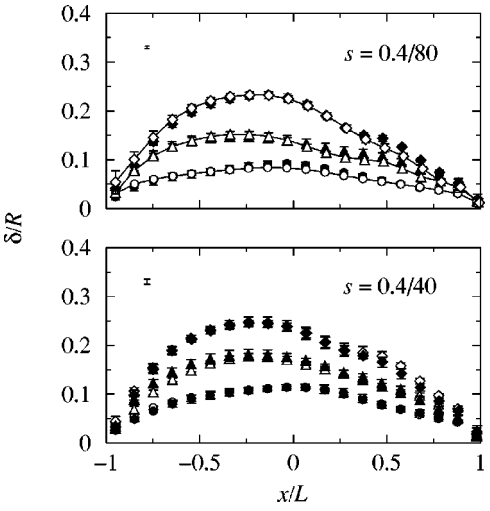

FIG. 12. Scaled layer thickness profiles for sand particles. Symbols denote experimental data for different Froude numbers (Fr) and fixed size ratio (s): ○, Fr$=2\times10^{-3}$; △, Fr$=22\times10^{-3}$; and ◇, Fr$=64\times10^{-3}$. Open symbols, $R=4$ cm; filled symbols, $R=8$ cm; open symbols with solid line, $R=16$ cm. The bar indicates the size of a particle.

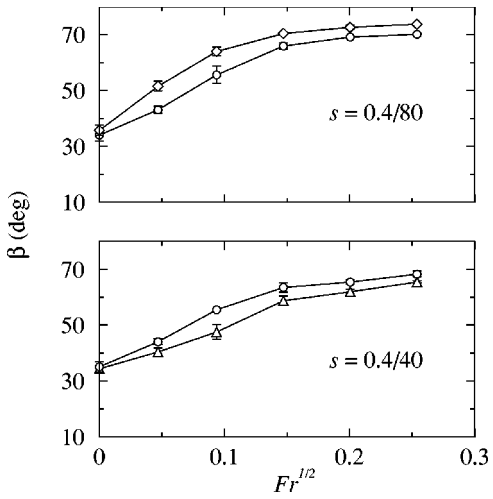

FIG. 13. Variation of the dynamic angle of repose (β) with dimensionless rotational speed ($\mathrm{Fr}^{1/2}$) for different size ratios (s). Symbols denote experimental data for sand particles rotated in cylinders of three different radii: △, $R=4$ cm; ○, $R=8$ cm; and ◇, $R=16$ cm.

the collisional viscosity (α_S) yields the following equation for the shear stress at the bed layer interface

$$\tau_{xy}=-M\rho\delta d\left(\frac{dv_x}{dy}\right)^2-\rho g\delta\cos\beta\tan\beta_s, \qquad (11)$$

where ρ is the bulk density in the flowing layer. The equation is of the same form as that given in Ref. [16] but in addition, gives the dependence of the shear stress on the particle size as well as the numerical value of the constant prefactor (M) in the collisional stress term.

Consider next a qualitative analysis of the observed behavior in terms of the model of Khakhar *et al.* [16]. All quantities in the following discussion are understood to be dimensionless, as defined in Sec. II. The parameter A/Fr gives the magnitude of the net gravitational driving force (gravity force less friction) and α_S determines the resistance due to collisional viscosity. The results given above indicate that α_S depends only on size ratio. Further, there is a near-linear

TABLE I. Normalized standard deviation (σ_δ/d) of layer thickness profiles from the corresponding averaged master curve for each Froude number (Fr) and size ratio (s).

	s	10^3Fr				
		2	9	22	40	64
Glass	1/80	0.32	0.35	0.34	0.33	0.32
	1/40	0.37	0.35	0.34	0.39	0.27
	1/20	0.17	0.15	0.10	0.08	0.16
Steel	1/80	0.21	0.33	0.33	0.34	0.46
	1/40	0.34	0.30	0.34	0.48	0.49
	1/20	0.17	0.05	0.11	0.16	0.06
Sand	0.4/40	0.17	0.50	0.49	0.25	0.37
	0.4/80	0.49	0.64	0.92	1.63	1.12

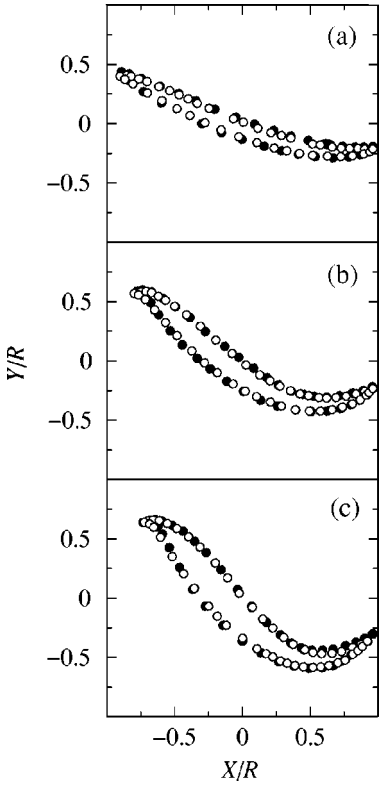

FIG. 14. Scaled layer shape profiles for 2 mm glass beads and steel balls rotated in cylinders of radius 16 cm for three different Froude numbers: (a) $\mathrm{Fr}=2\times10^{-3}$, (b) $\mathrm{Fr}=22\times10^{-3}$, and (c) $\mathrm{Fr}=64\times10^{-3}$. Filled symbols, glass beads; open symbols, steel balls.

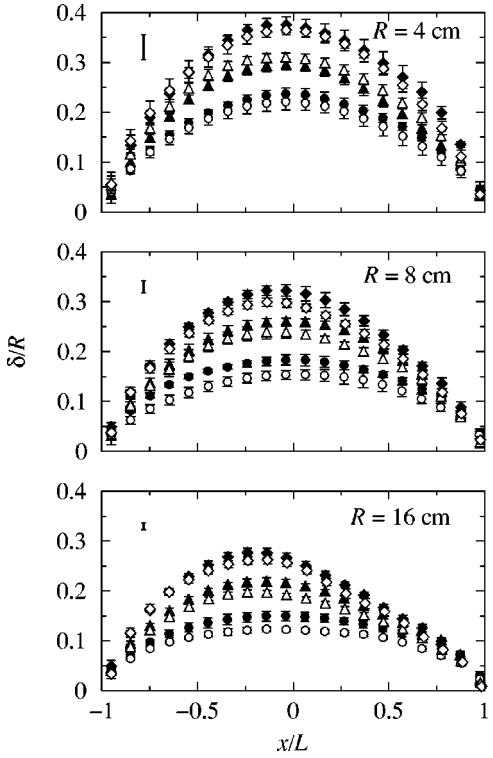

FIG. 15. Scaled layer thickness profiles for 2 mm glass beads and steel balls rotated in cylinders of three different radii (R). Symbols denote experimental data for different Froude numbers (Fr) and size ratios (s): ○, $\mathrm{Fr}=2\times10^{-3}$; and △, $\mathrm{Fr}=22\times10^{-3}$; ◇, $\mathrm{Fr}=64\times10^{-3}$. Filled symbols, glass beads; open symbols, steel balls. The bar indicates the size of a particle.

increase in the dynamic angle of repose (β) with rotational speed that gives $A\sim\sqrt{\mathrm{Fr}}$. Thus, with increasing rotational speed, the net driving force decreases ($A/\mathrm{Fr}\sim1/\sqrt{\mathrm{Fr}}$) while the collisional viscosity is constant. This results in lower average velocities and consequently higher maximum layer thicknesses with increasing rotational speeds, as observed. An increase in the Froude number also results in an increase of the relative magnitude of the term $\xi\overline{u^2}/\overline{Q}$ in Eq. (2). This is the only term in the momentum balance that is not symmetric with respect to ξ about the midpoint ($\xi=0$), and is the source of the skewness in the profiles. This term arises from the change in layer thickness with distance, and is the contribution to momentum change due to the particles entering and leaving the layer. In the upper part of the layer, the particles enter the layer from the bed at zero x velocity, which results in a decrease in the average velocity ($\overline{u}$); the reverse is true in the lower part of the bed. The flow rate ($\overline{Q}$) is symmetric about $\xi=0$, hence, $\overline{\delta}$ is higher in regions of lower velocity [Eq. (3)]. This results in profiles with greater thicknesses in the upper part of the layer ($\xi<0$) as compared to the lower part ($\xi>0$) because of the comparatively lower average velocity ($\overline{u}$) in the upper part. At very low Fr, the asymmetric term is negligibly small compared to the other terms, and hence, the profiles obtained are symmetric. Similarly, when the size ratio is smaller, the collisional viscosity (α_S) decreases, and thus, the asymmetric term becomes more dominant and the profiles are skewed as observed in the experiments. In the limit $s\to0$, $\alpha_S\approx0$ and the model reduces to that of Rao *et al.* [18] in which the resistance to flow is only due to friction.

The scaling of the model of Khakhar *et al.* [16] can be easily determined in terms of the dimensionless parameters of the model. Since the dynamic angle of repose does not scale with Fr and s, the parameter A also does not scale with Fr and s. Thus, for constant Fr and s the layer thickness profiles are different for the different systems. However, computations show that using the experimental values of β and β_s and the corresponding fixed values of Fr and s gives nearly identical computed layer thickness profiles, and the differences in the dynamic angles of repose have a relatively small effect. Thus, model predictions scale in the same way as the experimental results, to a good approximation.

Consider, finally, the predictions of the model for shape of the interface. Figure 20 shows the variation of the shear rate along the layer calculated using Eq. (9) for 2 mm steel balls in a 16 cm cylinder. The shear rate is nearly constant at the lowest Fr but at higher Fr, although the shear rate is nearly constant in the upper part of the layer ($\xi<0$) and close to the value at the low Froude number, there are significant deviations from constancy in the lower part of the layer ($\xi>0$). The cause of this deviation is not clear. Qualitatively similar profiles were obtained for glass beads and sand.

Figure 21 shows the calculated shear rate at the midpoint of the layer ($\dot{\gamma}_0$) from the layer thickness obtained experi-

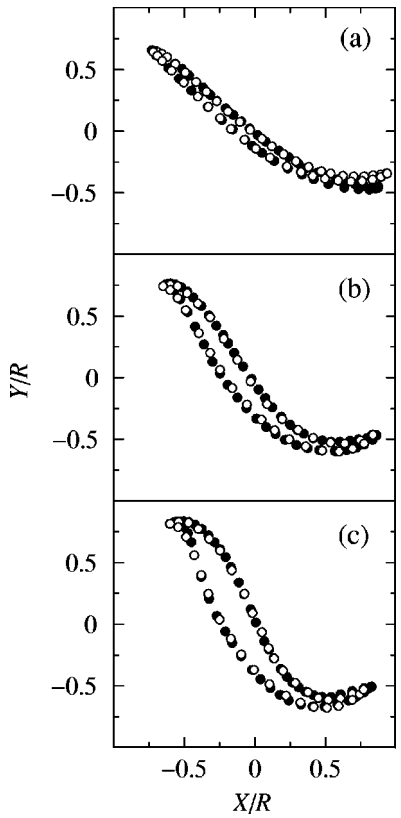

FIG. 16. Scaled layer shape profiles for 0.8 mm glass beads and sand particles rotated in cylinders of radius 16 cm for three different Froude numbers: (a) $\mathrm{Fr}=2\times10^{-3}$, (b) $\mathrm{Fr}=22\times10^{-3}$, and (c) $\mathrm{Fr}=64\times10^{-3}$. Filled symbols, glass beads; open symbols, sand particles.

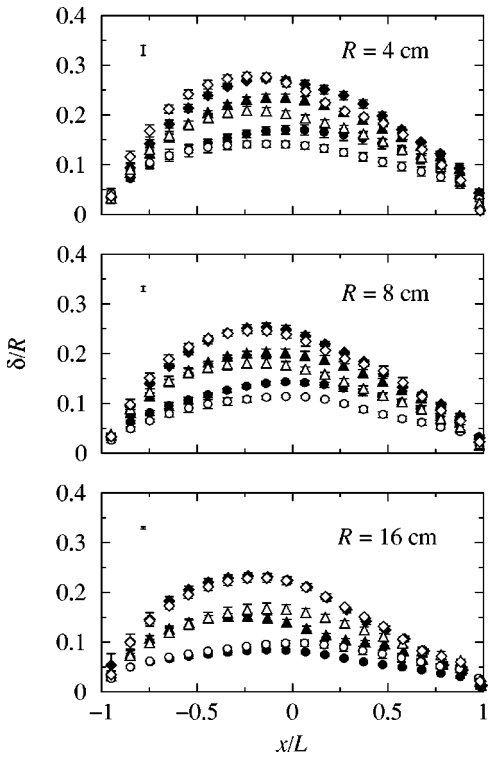

FIG. 17. Scaled layer thickness profiles for 0.8 mm glass beads and sand particles rotated in cylinders of three different radii. Symbols denote experimental data for different Froude numbers (Fr) and fixed size ratio (s): ○, $\mathrm{Fr}=2\times10^{-3}$; △, $\mathrm{Fr}=22\times10^{-3}$; and ◇, $\mathrm{Fr}=64\times10^{-3}$. Filled symbols, glass beads; open symbols, sand particles. The bar indicates the size of the particle.

mentally using Eq. (9) at $\xi=0$, for all the systems studied. The predicted shear rates at the midpoint [Eq. (8)]

$$\dot{\gamma}_0=\left[\frac{g\sin(\beta_0-\beta_s)}{Md\cos\beta_s}\right]^{1/2}, \tag{12}$$

where β_0 is the interface angle at the midpoint are also shown in Fig. 21. The scaling is very good for the steel balls but there is some scatter for the glass beads and sand particles. Using the scaling suggested by Rajchenbach [27] [Eq. (7)] results in the data falling in separate clusters for each particle size. The Rajchenbach [27] scaling results from the choice of the characteristic acceleration being $g\sin\beta$. Since $g\sin(\beta_0-\beta_s)\sim g(\tan\beta_0-\tan\beta_s)\cos\beta_0$, the above scaling [Eq. (12)] suggests that the net acceleration (gravity less friction) should be taken to be the characteristic value, where $g\tan\beta_s\cos\beta_0$ is the frictional contribution.

The scaling for the shear rate for different particle sizes and cylinder sizes reinforces our claim that end walls have little effect on the flow. A wide range of data collapses to a single curve considering the net driving force obtained using a macroscopic analysis based on flow in the bulk of the layer. Such a collapse for particles of different sizes would not occur if wall effects were significant.

From Eq. (10), we get $\beta_x=\beta_m$ at $\xi=0$, thus, the experimentally measured interface angle at the midpoint (β_0) is the maximum angle of repose. Figure 22 shows the variation of β_m with mass flow rate ($\dot{m}$) for 2 mm steel balls based on experiments at different Froude numbers and cylinder sizes. The mass flow rate is obtained from $\dot{m}=\rho u\,\delta T=\rho\omega R^2T/2$ [Eq. (3)] where T is the length of the cylinder and the bulk density is assumed to be $\rho=3200$ kg/m^3 based on measurements for the similar system reported in Ref. [26]. Data spanning nearly two decades of flow rate fall on a single curve, although with some scatter. Also shown in the figure are data for flow of 2 mm steel balls in a quasi-2D heap of the same thickness (T) [26]. There is a reasonable agreement between the two. These results indicate that it may be possible to correlate the maximum angle of friction with local flow rate in the layer and to use this to predict surface profiles. This is illustrated next.

Figure 23 shows a comparison between the measured interface angles (β_x) and the angles predicted from Eq. (10). The experimentally measured values of β_m and $\overline{\delta}(\xi)$ are used in the calculation and there are no fitting parameters. There is reasonable agreement between the theory and experiment except at highest Fr. The deviations could be due to curvature effects that are not accounted for in the model and could lead to errors in the estimation of the shear rate. Wall friction effects would also introduce errors in measurement of both β_x and β_m. Notice that the surface angle becomes negative for both experiments and theory at high Fr. This corresponds to a turning up of the interface at the end of

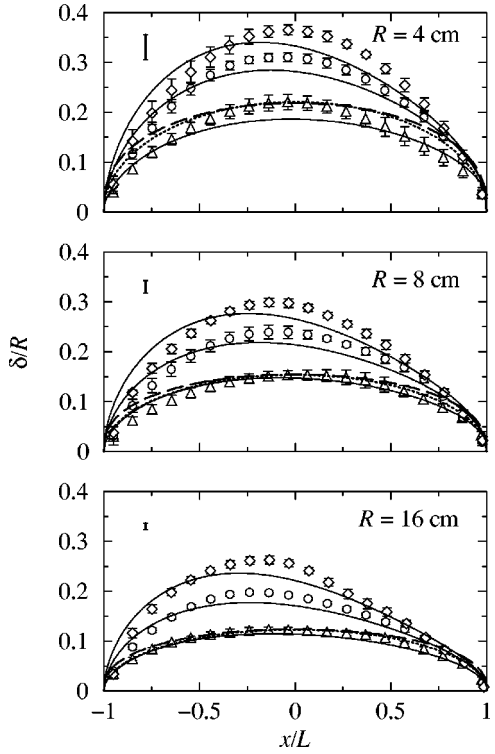

FIG. 18. Layer thickness profiles for 2 mm steel balls. Symbols denote experimental data for three different Froude numbers (Fr): △, Fr$=2\times10^{-3}$; ○, Fr$=22\times10^{-3}$; and ◇, Fr$=64\times10^{-3}$. Solid lines are predictions of the model of Khakhar *et al.* [16]. Dotted lines are the predictions of the model of Makse [21]. Dashed lines are the predictions of the model of Elperin and Vikhansky [20]. The bar indicates the size of a particle.

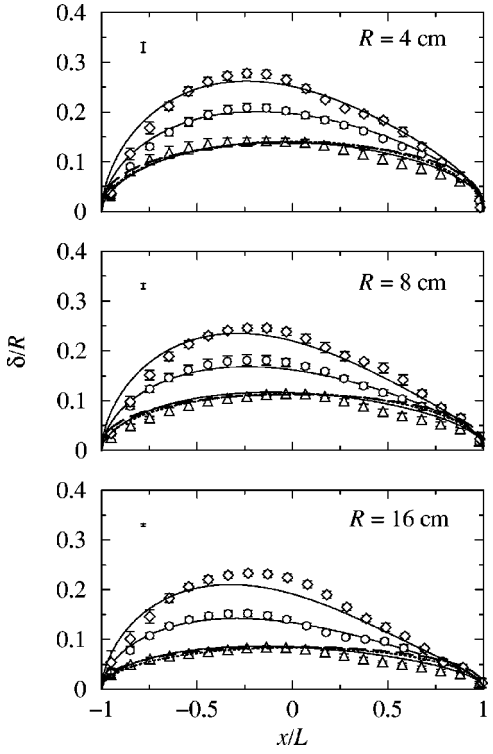

FIG. 19. Layer thickness profiles for 0.8 mm sand particles. Symbols denote experimental data for three different Froude numbers (Fr): △, Fr$=2\times10^{-3}$; ○, Fr$=22\times10^{-3}$; and ◇, Fr $=64\times10^{-3}$. Solid lines are predictions of the model of Khakhar *et al.* [16]. Dotted lines are the predictions of the model of Makse [21]. Dashed lines are the predictions of the model of Elperin and Vikhansky [20]. The bar indicates the size of a particle.

the layer producing the characteristic *S* shape. Similar behavior is obtained for glass beads and sand.

The factors that generate the *S*-shaped profile can be understood, qualitatively, from Eq. (10). Since the mass flow rate decreases with distance from the midpoint, β_m also decreases with distance from the midpoint. Thus, the first term on the right-hand side of Eq. (10) is maximum at the midpoint and decreases with distance from the midpoint. The second term in the equation is positive in the upper part of the layer ($\xi<0$), and, thus, β_x is larger than β_m and increases with distance from the midpoint. In the lower part of the layer, the reverse is true and β_x is less than β_m. In fact, for higher Fr, for which high $\dot{\gamma}$ values are obtained (Fig. 20) the angle becomes negative (layer turns up) producing the characteristic *S* shape found in the experiments.

The results presented here indicate that the continuum model of Khakhar *et al.* [16] gives a good prediction of the flow in the layer. Specifically, the stress constitutive equation used seems to work well for a wide range of parameters. The scaling for the shear rate also indicates that $\tan\beta_s$ may be a good estimate for the effective coefficient of dynamic friction for the flow. The predictions of the extension of the heap models for the interface angle are reasonable, though in this case, the results are affected by end-wall friction effects that are unavoidable in the flow visualization technique used here.

V. CONCLUSIONS

Experimental results for the flow in rotating cylinder, obtained by flow visualization, are presented for a wide range of systems and rotational speeds. The major results are first summarized below. The surface flowing layer is found to become thicker and more *S* shaped with increasing Froude number. As the size ratio is decreased, the layer becomes

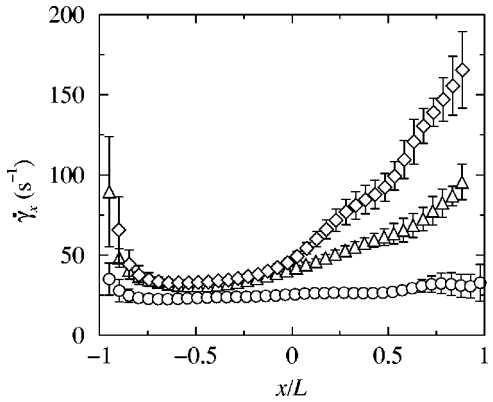

FIG. 20. Variation of the computed shear rate along the flow direction for 2 mm steel balls in a cylinder of radius $R=16$ cm. Symbols show data for three different Froude numbers (Fr): ○, Fr$=2\times10^{-3}$; △, Fr$=22\times10^{-3}$; and ◇, Fr$=64\times10^{-3}$.

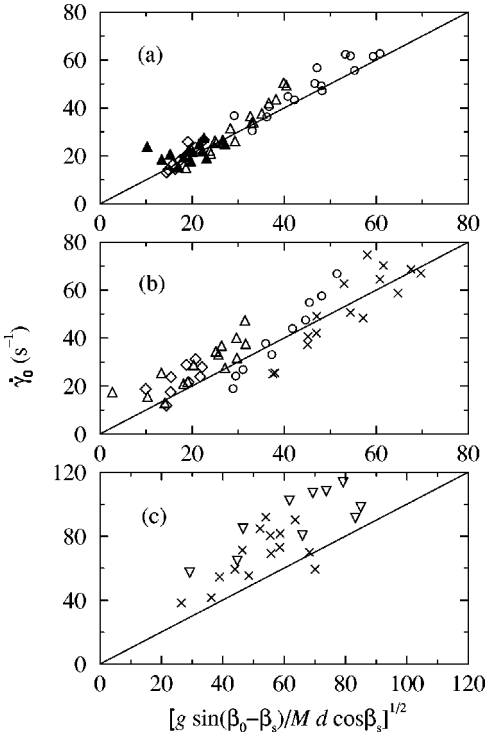

FIG. 21. Variation of the computed shear rate at the midpoint ($\dot{\gamma}_0$) for different size ratios and Froude numbers versus the characteristic shear rate $[g \sin(\beta_0-\beta_s)/Md \cos \beta_s]^{1/2}$ for all particles. (a) Steel balls, (b) glass beads, and (c) sand particles. Symbols denote data for different sized particles: ○, $d=1$ mm; △, $d=2$ mm; ◇, $d=4$ mm; ▽, $d=0.4$ mm; and ×, $d=0.8$ mm. Solid lines are predictions of Eq. (12). Filled symbols indicate the data obtained for the open heap experiments [26].

more *S* shaped and the scaled layer thickness decreases. The layer thickness profiles are symmetric at low-Froude numbers and high-size ratio and become increasingly skewed with increasing Fr and decreasing *s*, with the maximum point shifting to the upper parts of the layer ($x<0$). The dynamic angle of repose increases monotonically with rotational speed showing a near-linear dependence in all cases. For a fixed Froude number and particle size, the angle of repose increases with the cylinder size. The dynamic angles of repose are, by and large, higher for the smaller particles when the other parameters are held fixed. At the same Froude number, size ratio, and cylinder size, the dynamic angles of repose are higher for the sand particles than steel balls or glass beads, which are comparable.

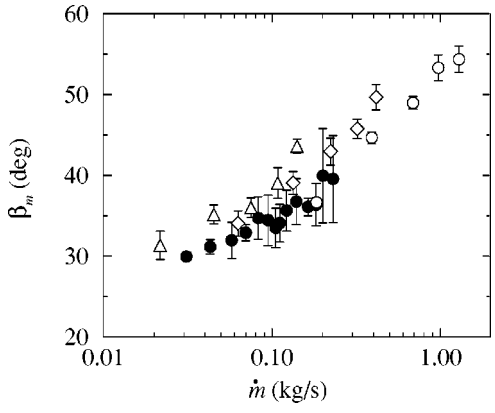

FIG. 22. Variation of the maximum angle of repose (β_m) with the mass flow rate ($\dot{m}$) for 2 mm steel balls. Open symbols show data obtained in three different sizes of cylinders. △, $R=16$ cm; ◇, $R=8$ cm; and ○, $R=4$ cm. Filled symbols indicate the data obtained for the open heap experiments [26].

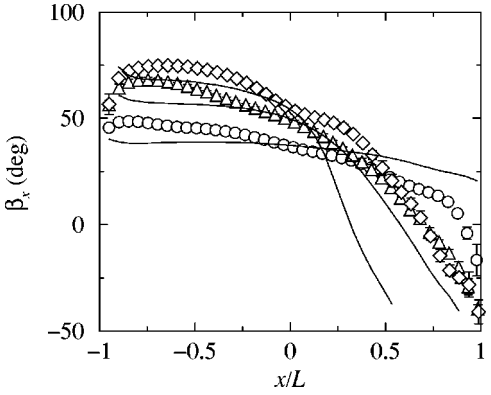

FIG. 23. Variation of the interface angle (β) along the flow direction for 2 mm steel balls in cylinder of radius $R=16$ cm. Symbols show data for three different Froude numbers (Fr): ○, $\mathrm{Fr}=2\times10^{-3}$; △, $\mathrm{Fr}=22\times10^{-3}$; and ◇, $\mathrm{Fr}=64\times10^{-3}$. Solid lines are the predictions of Eq. (10).

Scaling analysis shows that the flow in the layer depends primarily on the Froude number and size ratio. Other parameters such as interparticle coefficients of friction and elasticity have a secondary effect. The scaling is also found to be nearly independent of material type for the limited range of materials considered. In all cases, the details of the shapes of the scaled layer profiles are nearly identical and good quantitative agreement is shown for the scaled layer thickness profiles. The dynamic angles of repose, however, do not scale with Fr and *s*.

The scaling results are of direct utility for engineering design based on ''scale up.'' In this approach, large-scale systems are built based on the experimental results obtained from small systems, using scale-up rules. For applications involving flow in a cylinder, results of this paper indicate that size ratio and Froude number should be kept constant while scaling up. The results are also useful for testing other theories.

Comparison of the predictions of continuum theories to experimental results shows their range of utility. The predictions of the theories of Elperin and Vikhansky [20] and Makse [21] are nearly identical and show good agreement with experimental data for the layer thickness profiles at low Fr; both theories have one fitting parameter. The model of Khakhar *et al.* [16] gives good predictions (deviations less than one-particle diameter in most cases) over the entire range of parameters studied, based on an empirical correlation for the fitting parameter (α_S) obtained from the data. Additional inputs to the model are the static and dynamic angles of repose, which are measured. The data fitting also yields an empirical constitutive equation for the shear stress for the surface flows that appears to be valid for wide param-

eter ranges. Qualitative analysis of the model gives an understanding of the behavior observed with variation of Fr and *s*. The model is simple and has wide applicability. Including the effects of layer curvature and dilation would improve predictions, particularly at high Fr.

Further analysis of the data using the model indicates that the shear rate is nearly constant along the layer at low Fr, but this constancy does not hold at high Fr particularly in the lower part of the layer ($x>0$). Data for all the systems studied indicate that the shear rate at the midpoint scales as $\dot{\gamma}_0 = [g \sin(\beta-\beta_s)/Md \cos\beta_s]^{1/2}$, suggesting that the scaling is material independent. This scaling also indicates that the frictional resistance in the flow is well described by the coefficient of friction $\tan\beta_s$. Finally, predictions of the layer interface angles using an extension of the BRdG model [24] are in reasonable agreement with experimental data except at high Froude numbers.

We conclude with a discussion of experimental technique used in this paper. The primary merit of the flow visualization technique is its simplicity: quite detailed studies of the flow are possible without sophisticated instruments. Yet, as mentioned above, wall effects are unavoidable since the measurements are based on motion adjacent to the transparent wall. The experimental results for different cylinder lengths, as well as the scaling results indicate that the details of the flow are unaffected by the wall. However, the angle of repose, which is sensitive to shape, roughness, and other particle properties, is affected by cylinder lengths and wall friction. A very detailed study of surface angles is thus not accessible to flow visualization experiments and requires noninvasive measurements in long cylinders, for example, using MRI. The results presented here, however, provide a starting point for the analysis of surface shapes in a rotating cylinder flow, which are important in several phenomena, for example, surface flow driven segregation [19]. In light of the scaling results obtained, it would be interesting to investigate scaling in more complex systems such as scaling in radially segregating systems [28,29] and in tumbled systems with noncircular cross sections [30,31], in which the flow is time periodic.

ACKNOWLEDGMENT

The financial support of Department of Science and Technology, India through the Swarnajayanti Fellowship project (DST/SF/8/98) is gratefully acknowledged.

[1] P. G. de Gennes, Rev. Mod. Phys. **71**, S374 (1999).
[2] C. S. Campbell, Annu. Rev. Fluid Mech. **22**, 57 (1990).
[3] H. M. Jaeger, S. R. Nagel, and R. P. Behringer, Rev. Mod. Phys. **68**, 1259 (1996).
[4] J. Duran, *Powder and Grains* (Springer-Verlag, New York, 2000).
[5] G. H. Ristow, *Pattern Formation in Granular Materials* (Springer, Berlin, 2000).
[6] B. J. Ennis, J. Green, and R. Davis, Chem. Eng. Prog. **90**, 32 (1994).
[7] J. Bridgewater, Chem. Eng. Sci. **50**, 4081 (1995).
[8] J. M. Ottino and D. V. Khakhar, Annu. Rev. Fluid Mech. **32**, 55 (2000).
[9] H. Henein, J. K. Brimacombe, and A. P. Watkinson, Metall. Mater. Trans. B **14B**, 191 (1983).
[10] J. Rajchenbach, Phys. Rev. Lett. **65**, 2221 (1990).
[11] C. M. Dury, G. H. Ristow, J. L. Moss, and M. Nakagawa, Phys. Rev. E **57**, 4491 (1998).
[12] K. Yamane, M. Nakagawa, S. A. Altobelli, T. Tanaka, and Y. Tsuji, Phys. Fluids **10**, 1419 (1998).
[13] R. Khosropour, E. Valachovic, and B. Lincoln, Phys. Rev. E **62**, 807 (2000).
[14] M. Nakagawa, S. A. Altobelli, A. Caprihan, E. Fukushima, and E. K. Jeong, Exp. Fluids **16**, 54 (1993).
[15] J. Rajchenbach, E. Clément, and J. Duran, Mater. Res. Soc. Symp. Proc. **367**, 525 (1995).
[16] D. V. Khakhar, J. J. McCarthy, T. Shinbrot, and J. M. Ottino, Phys. Fluids **9**, 31 (1997).
[17] A. A. Boateng and P. V. Barr, J. Fluid Mech. **330**, 233 (1997).
[18] S. J. Rao, S. K. Bhatia, and D. V. Khakhar, Powder Technol. **67**, 153 (1991).
[19] O. Zik, D. Levine, S. G. Lipson, S. Shtrikman, and J. Stavans, Phys. Rev. Lett. **73**, 644 (1994).
[20] T. Elperin and A. Vikhansky, Europhys. Lett. **42**, 619 (1998).
[21] H. A. Makse, Phys. Rev. Lett. **83**, 3186 (1999).
[22] R. A. Bagnold, Proc. R. Soc. London, Ser. A **255**, 49 (1954).
[23] J. P. Bouchaud, M. E. Cates, J. Ravi Prakash, and S. F. Edwards, J. Phys. I **4**, 1383 (1994).
[24] T. Boutreux, E. Raphaël, and P. G. de Gennes, Phys. Rev. E **58**, 4692 (1998).
[25] S. Douady, B. Andreotti, and A. Daerr, Eur. Phys. J. B **11**, 131 (1999).
[26] D. V. Khakhar, A. V. Orpe, P. Andresén, and J. M. Ottino, J. Fluid Mech. **441**, 355 (2001).
[27] J. Rajchenbach, in *Physics of Dry Granular Media*, edited by H. Hermann (Kluwer Academic, Dordrecht, 1998), p. 421.
[28] D. V. Khakhar, J. J. McCarthy, and J. M. Ottino, Phys. Fluids **9**, 3600 (1997).
[29] L. Prigozhin and H. Kalman, Phys. Rev. E **57**, 2073 (1998).
[30] D. V. Khakhar, J. J. McCarthy, J. F. Gilchrist, and J. M. Ottino, Chaos **9**, 195 (1999).
[31] K. M. Hill, D. V. Khakhar, J. F. Gilchrist, J. J. McCarthy, and J. M. Ottino, Proc. Natl. Acad. Sci. U.S.A. **96**, 11701 (1999).